Large eddy simulation of the tidal power plant Deep Green using the actuator line method

[a]Sam T. Fredriksson*, [a]Göran Broström, [b]Marcus Jansson, [c]Håkan Nilsson, and [b]Björn Bergqvist

[a]Department of Marine Sciences. University of Gothenburg, Gothenburg, Sweden
[b]Minesto AB, Gothenburg, Sweden
[c]Department of Mechanics and Maritime Sciences, Chalmers University of Technology, Gothenburg, Sweden
*Contact author: sam.fredriksson@gu.se

Abstract— **Tidal energy has the potential to provide a substantial part of the sustainable electric power generation. The tidal power plant developed by Minesto, called Deep Green, is a novel technology using a 'flying' kite with an attached turbine, moving at a speed several times higher than the mean flow. Multiple Deep Green power plants will eventually form arrays, which requires knowledge of both flow interactions between individual devices and how the array influences the surrounding environment. The present study uses large eddy simulations (LES) and an actuator line model (ALM) to analyze the oscillating turbulent boundary layer flow in tidal currents without and with a Deep Green power plant. We present the modeling technique and preliminary results so far.**

Keywords— Tidal energy, Turbulence, Large Eddy Simulation (LES), Actuator Line Method (ALM).

I. INTRODUCTION

There are several new technologies emerging for extracting power from tidal currents. They span from turbines mounted on the bottom to devices that operates in mid-depth or at the surface [1]. The fact that the power plants will be mounted in regions with strong tidal currents implies that robust design of the equipment becomes an important issue. The tidal current in itself is quite well-known and easy to observe, but the small-scale turbulent fluctuations are less known and more demanding to observe. One way to describe the turbulence fields and their impact on the structure is to use computational fluid dynamic modelling.

There are some studies that have targeted the turbulence characteristics of tidal currents [2-4]. There are also some studies focusing on how bottom mounted turbines operate in a tidal flow [5-7]. The main part of the studies have focused on turbulence intensity and length scale of the turbulent eddies, but other quantities such as structure functions, probability density functions, intermittency, coherent turbulence kinetic energy, anisotropy invariants, and a scalar measure of anisotropy to characterize the turbulence have been suggested as well [8].

Power plants reduce the velocity behind the plants, creating a wake in the flow field. The wakes for atmospheric wind mills and wind farms have been extensively studied [9, 10]. It has been found that the return to normal flow conditions, e.g. turbulent fluctuations, depends on e.g. how rough the ground is and that it is faster over rough land than over smooth seas. For land-based wind farms it has become evident that they increase the mixing in the lower atmosphere [11, 12]. For offshore wind farms it has been found that the wind wake may force local up- and down-welling [13]. It can be argued that horizontal mixing is more important than vertical mixing in shallow water conditions as compared to the atmospheric counterpart. This fundamental difference between the (shallow and coastal) ocean and the atmosphere probably increases the importance of how tidal power plants should be placed in relation to each other and how they affect the surrounding area, as compared to wind farms. Today there are few studies, e.g. [14-17], of those aspects of the energy extraction from ocean currents.

A. Deep Green technology

The Deep Green power plant is a novel marine energy technology that produces electricity from tidal and/or ocean currents. The main components of the Deep Green, shown in Fig. 1, are the wing, the axial turbine, the nacelle that comprises the generator and power electronics, and the rudders. The Deep Green is attached to a foundation on the seabed via three struts and a long tether. The control system steers the power plant in a predefined trajectory. In its current design, the length of the wing is 12 meters and the rated power of the generator is 500 kW. Multiple Deep Green devices will be placed together to form an array.
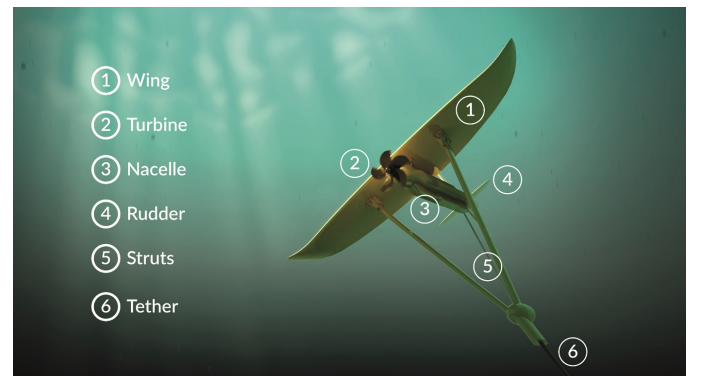

Fig. 1. Illustration of the Deep Green device.

The Deep Green technology has the same working principle as a wind kite. The wing hydrodynamics enables the power plant to accelerate several times the speed of the flow, moving almost perpendicular to the flow. Accordingly, the Deep Green power plant can operate in low-flow stream and use less material in construction compared to other similar technologies, in relation to the installed capacity.

The Deep Green is preprogrammed to fly in an 8-shaped trajectory, see Fig. 2, while the water is pressed through the

rotating turbine. A generator in the nacelle converts the turbine rotation to electricity which is transferred via the tether and the internal network to the grid.
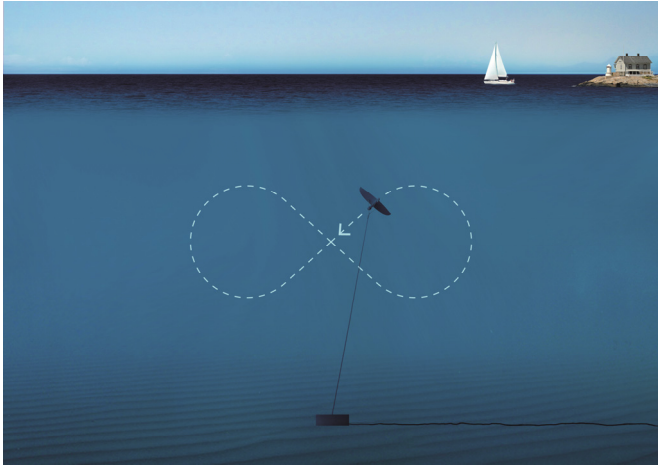

Fig. 2. Sketch of the trajectory of the Deep Green.

Minesto is using a combination of in-house, open source and commercially available computational codes to perform CFD, rigid body and multi body simulations in the design work of the Deep Green technology. The present study gives an opportunity to better understand the underlying energy resource, i.e. the tidal flow of water. With a more realistic turbulent flow as input to the simulations, the dimensioning of components can be made with better accuracy. Studies of how the Deep Green device affects the turbulent flow downstream will be a valuable input to coming array designs.

B. The present study

The present paper consists of a methods section where the set-up of the simulations and the actuator line method is described. This is followed by a results section that focuses on the preliminary results, comparing the flow fields and turbulent structures with and without the Deep Green. In the last section we present our conclusions and future work.

II. METHODS

This section presents the work process and the numerical set-up, followed by a description of the actuator line model (ALM).

A. Work process

The site in the presents study is approximately 80 m deep with a maximum temporal peak of the vertically averaged flow of about 1.6-2.4 ms^{-1} depending on the tidal acceleration variability. Initial studies show that the tidal flow is a strongly forced accelerating current, and that the turbulence fields are not close to be in a quasi-stationary state with the mean flow, but rather depends on the phase in the tidal cycles.

The present study is therefore divided in three steps:

1. Full tidal cycle large eddy simulations (LES) to both give information of the free turbulence characteristics and to produce initial conditions for precursor simulations. This is done without Deep Green, with horizontally cyclic boundary

conditions and a time-varying force term that drives the flow.

2. Precursor LES to produce initial flow conditions and inlet boundary conditions for Deep Green simulations. This is done without Deep Green, with initial conditions from step 1 and a time-varying source term that drives the flow. The simulation is started at the instance in time, t_0, where the flow corresponds to a prior dynamics analysis in Dymola.

3. LES using precursor initial and inlet boundary conditions, including Deep Green where the wing and the turbine are modeled using an actuator line model technique. The precursor inlet boundary condition here determines the flow rate by setting the velocity, the sub-grid scale turbulent kinetic energy, and the turbulent viscosity. A Neumann boundary condition is used at the outlet.

Fig. 3 and TABLE I. show the computational domain and details about the three steps. The tidal cycle simulation in step 1 is performed using a pseudo-spectral method (pseudo-spectral in the horizontal direction and finite differences in the vertical direction). The method is available in a code herein referred to as NCAR-LES which targets geophysical turbulence [18-20]. The pseudo-spectral method allows accurate and fast execution but requires horizontally cyclic conditions. Initial studies in the present work show that the length scale of the turbulence is on the order of 100-150 m in the flow direction. In order to avoid locking of the large-scale turbulence structures due to the horizontally cyclic conditions we use a model domain spanning some 10 times this value in step 1 [21]. The turbulent structures are resolved down to a fraction of the length of the Deep Green structure, which has a wing span of 12 m. The aim of the precursor study (step 2) is to deliver inlet boundary conditions for the Deep Green simulation (step 3). It is performed using the OpenFOAM CFD solver and is an intermediate step that has the purpose of preparing step 3. OpenFOAM is a general-purpose finite volume solver to which an actuator line model can be attached [14, 22, 23]. It is not as efficient as NCAL-LES for the simulations in step 1, but it does not require cyclic conditions and it can be used for the arbitrary geometries that will be of interest in future work. In step 2 the results from step 1 at the time instance t_0 is used as the initial conditions, see Fig. 6. t_0 is in the accelerating tidal phase, starting just before the peak flow rate. It is chosen at the time when the vertically averaged velocity over the depth of the trajectory of the Deep Green corresponds to the plug flow of $1.6\ ms^{-1}$ that was used in a previous Dymola simulation that was performed to find e.g. the trajectory path. The step 2 simulation is driven by the time-varying tidal body force for 400 s while sampling the fluctuating velocity and sub-grid scale properties at the inlet boundary for every time step of the simulation. These temporally and spatially varying fields are then used as upstream boundary conditions for the step 3 simulation. The step 3 simulation starts at the same instance in time, t_0, as that of step 2, using the same initial conditions as in step 2 but the sampled time-varying velocity, sub-grid scale turbulent kinetic energy, and the turbulent viscosity of step 2 are applied as the

upstream boundary conditions. The Deep Green plant is in step 3 modeled using the actuator line method, in which source terms are added to the momentum equations. Those source terms are based on separate studies of lift and drag coefficients, and the flight path is taken from a previous simulation using the Dymola software. At this stage it is thus only the flow that is affected by Deep Green, and not vice versa. The previous Dymola simulations are the opposite – the flight path is determined by the forces from the flow, but for a constant plug flow. It should be noted that the simulations in steps 2 and 3 are only performed for a short duration of real time, in the accelerating phase of the tidal flow, close to the maximum velocity. Further, the domain size is smaller than in step 1, however using the same mesh resolution. It is nevertheless assumed that the turbulent flow field of step 3 is representative enough for the purpose of that simulation at this stage. All such aspects will be addressed in future work. We have used the same time step in the step 2 and step 3 simulations.
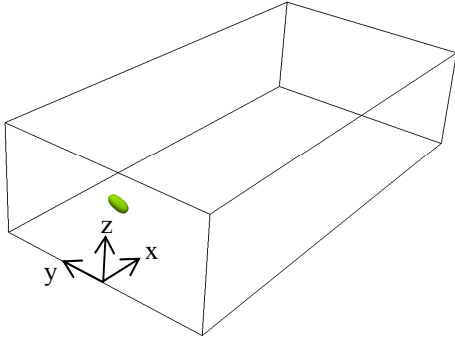

Fig. 3. Sketch of computational domain where the Deep Green is indicated at the center of its trajectory, close to the upstream boundary.

TABLE I. CODE, COMPUTATIONAL DOMAIN, MESH RESOLUTION AND FORCES

Step	Description	Code	Domain[1]	Resolution[2]	Force
1	Tidal cycle	NCAR-LES	16, 4, 1	2048, 512, 128	F_T
2	Precursor	OpenFOAM	4, 2, 1	512, 256, 128	F_T
3	Deep Green	OpenFOAM	4, 2, 1	512, 256, 128	F_{DG}

[1] Size relative to depth, $H = 80\ m$, in x, y, and z directions.

[2] In x, y, and z directions (equidistant).

B. Numerical set-up

The filtered Navier-Stokes equations used in the large eddy simulations are written as

$$\frac{\partial \tilde{u}_i}{\partial x_i} = 0 \tag{1}$$

$$\frac{\partial \tilde{u}_i}{\partial t} + \frac{\partial \tilde{u}_i \tilde{u}_j}{\partial x_j} = -\frac{1}{\rho}\frac{\partial \tilde{p}}{\partial x_i} + \nu\frac{\partial^2 \tilde{u}_i}{\partial x_j \partial x_j} - \frac{\partial \tau_{ij}}{\partial x_j} + \frac{F_{T,i}}{\rho} + \frac{F_{DG,i}}{\rho} \tag{2}$$

where $\tilde{u}$ and $\tilde{p}$ stand for the filtered velocity and pressure respectively and ρ is the density assumed to be constant. t is time, x_i is the $x, y,$ and z directions. τ_{ij} is the sub-grid scale stress tensor modeled via the one-equation eddy-viscosity concept, using a transport equation for the sub-grid scale kinetic energy and a local length scale [24, 25]. $F_{T,i}$ and $F_{DG,i}$ are body forces to mimic the tidal forcing (T) and the actuator line model describing the Deep Green effect (DG), respectively. We have in equation (2) not included the effects of buoyancy, which can enhance or depress turbulence depending on its sign, as well as the effects of Coriolis forces caused by the rotation of the earth. The body force

$$F_{T,i} = f_T \cos(\omega t)\mathbf{e}_x \tag{3}$$

is activated during the tidal cycle and precursor simulations (steps 1 and 2) and deactivated during the Deep Green simulations (step 3). Here f_T is the amplitude, $\omega = 2\pi/t_0$ with the period t_0 set to 12 hours, and $\mathbf{e}_x$ denotes the unit vector in the x direction (general flow direction). The force from Deep Green, $F_{DG,i}$, (further discussed below) is only activated during the Deep Green simulations (step 3).

We apply cyclic boundary conditions in both horizontal directions for the tidal cycle and precursor simulation (steps 1 and 2), but only in the y-direction for the Deep Green simulation (step 3). In step 3, Neumann and Dirichlet boundary conditions are applied for the pressure at the upstream ($x = 0$) and downstream boundary ($x = 4H$), respectively. For the velocity and sub-grid scale properties we apply a temporal and spatial varying boundary condition, given by the precursor simulation, at the upstream boundary, and Neumann boundary condition at the downstream boundary. The bottom boundary condition is given as a rough wall condition with a bottom roughness parameter z_0=0.01 m in all simulations.

C. Actuator Line Model

The Deep Green plant is taken into account in step 3 using the actuator line model [26], where the body forces, see Fig. 4, that arise due to the Deep Green are determined using a blade-element approach. An actuator line model is used since it is not possible to resolve the components of Deep Green and the resulting small-scale structures in a domain that is large enough to also cover the largest scales. Here the wing and the axial turbine is modeled. The wing is discretized in the spanwise direction using 10 elements, in combination with two-dimensional airfoil characteristics. The turbine is modeled with one element with a small size compared to the mesh size resulting in a source that can be considered to be a point source. In the following the word "foil" will be used as the general term for the modeling of both the wing and the turbine. Denoting the velocity (in vector notation) of a foil as $\mathbf{v}_f$ and the flow field velocity at the leading edge of the foil as $\mathbf{u}_{LE}$, the local flow velocity relative to the foil is given by

$$\mathbf{u}_{rel} = \mathbf{u}_{LE} - \mathbf{v}_f. \tag{4}$$

The angle of attack is found as

$$\alpha = sin^{-1}\left(\mathbf{e}_{wingPlaneNormal} \times \mathbf{e}_{rel}\right) \tag{5}$$

where $\mathbf{e}_{wingPlaneNormal}$ and $\mathbf{e}_{rel}$ denote the unit vector along the normal to the wing plane defined by the chord line and the span direction of the foil and the unit vector along the relative velocity, respectively, and $\times$ denotes the cross product. The three-dimensional actuator line force per spanwise unit length is calculated as

$$F_{foil,i} = \frac{1}{2}\rho U_{rel}^2 c(C_L\mathbf{e}_L + C_D\mathbf{e}_D) \quad (6)$$

where c is the chord length, $C_L = C_L(\alpha, Re)$ and $C_D = C_D(\alpha, Re)$ are the lift and drag coefficients respectively given in lookup tables. $\mathbf{e}_L$ and $\mathbf{e}_D$ denote the unit vectors in the lift and drag directions.
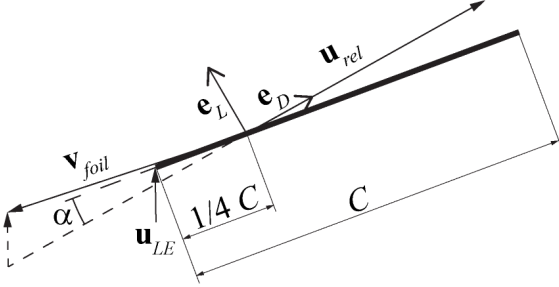

Fig. 4. Sketch of a foil with chord length C.

$\mathbf{v}_f$ and the position, and the orientation of the foil are given as an input from a prior simulation performed in the software Dymola that models the complete Deep Green including the control system, but for a plug flow only. This input is given and the forces are projected back to the flow at a position $1/4$ chord downstream the leading edge along the chord. We have chosen to have a distance between this point and the sampling point of the field velocity (leading edge) to decrease the influence of the source term on the sampled velocity. In order to avoid numerical oscillations due to steep gradients, the body force (source term) is projected by means of a spherical Gaussian function as [26]

$$F_{DG,i}(\mathbf{r}) = \frac{F_{foil,i}}{\varepsilon^3\pi^{3/2}}exp\left[-\left(\frac{|\mathbf{r}|}{\varepsilon}\right)^2\right] \quad (7)$$

where $\mathbf{r}$ is the vector between the cell where the source is to be applied and the actuator point, and ε controls the Gaussian width. Here the Gaussian widths are individually determined for each actuator element at each time step as the largest value out of three alternative formulations based on the 1) lift as a function of the chord length as $\varepsilon_{chord} = c_{chord}C$ where $c_{chord} = 1/4$, 2) mesh size as $\varepsilon_{mesh} = c_{mesh}2\Delta x$ where $c_{mesh} = 2$ and the cell length $\Delta x = \sqrt[3]{V_{cell}}$ is related to the cell volume, and 3) drag as $\varepsilon_{drag} = c_{drag}C_dC/2$ [23]. The thrust of the turbine is modeled similar to (6) using the thrust coefficient C_T instead of C_D, applying an element spanwidth smaller than the local mesh size.

The lift and drag coefficients have been determined by steady state analyses for a complete wing while varying the angle of attack. The coefficients are determined for ten sections as presented in Fig. 5. Here the $k - \omega$ turbulence model was used and the flow velocity was $12\,ms^{-1}$. The Reynolds number, $Re = U_{rel}c/\nu$, is fairly stable during the trajectory of Deep Green, and it is known [27] that the lift and drag coefficients are fairly insensitive to Re for high enough Re. Hence, the possibility to express the lift and drag coefficients as a function of Re has not been used in this study. When two-dimensional airfoil data is used, it needs in general to be corrected for three-dimensional effects such as infinite span width and skew attack velocity in relation to the chord direction [26]. No correction for a finite-span is however needed in this study since the lift and drag coefficients have been determined using the actual three-dimensional finite wing. A correction due to skew inflow is a subject for future improvement once the data is available.
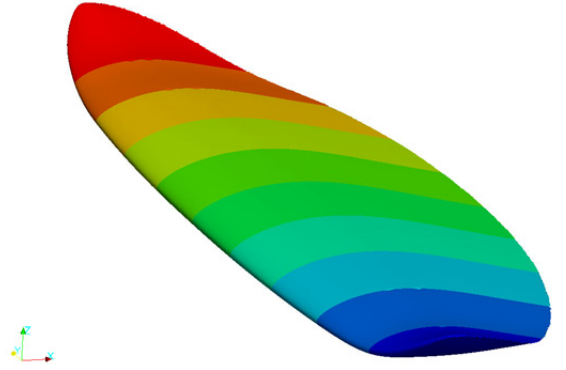

Fig. 5. Sections of the wing where the fores were determind in the steady state analysis.

This work is based on the libraries of turbinesFoam [23], which is distributed as a stand-alone user-contributed module for OpenFOAM. The libraries allow the ALM to be used through the fvOptions functionality in OpenFOAM. Our work has generalize the ALM to make it possible to prescribe an arbitrary path of the foils, not restricted to circular as typical for axial wind and tidal turbines [14]. In turbinesFoam there are a few features that we have chosen not to use or to investigate later on. These are 1) dynamic stall which isn't used since there is no risk for stall with the attack angles used in this study, 2) added mass which is used in conjunction to the dynamic stall correction, 3) flow curvature effect that arises due to a varying angle of attack along the chord direction which has not been taken into account in the present study since it is believed to only have a minor effect of the general behavior of the flow downstream of the foil following the prescribed path, and 4) end effects where we just started some sensibility studies that so far points in the direction of only minor influence of the downstream field.

III. RESULTS

The main emphasis here is to present some typical results for the Deep Green simulation. Studies of the domain size, resolution sensitivity and code comparison will therefore be presented elsewhere. We start, however, by briefly presenting

the results for the tidally driven simulation since this simulation gives the initial fields for the precursor study, which then in turn gives the initial conditions and inlet boundary conditions for the Deep Green simulation.

A. Tidal forcing

The volume averaged velocity during a tidal cycle simulation is shown as a function of time in Fig. 6. The maximum volume averaged velocity at the second tidal peak is about $2.1 \, ms^{-1}$. This specific case has not been run longer than shown in the figure, but simulations with a smaller domain with the same resolution show that the velocity at the third maximum is close to that at the second maximum, which shows that the second maximum is close to "fully developed". In a friction-free flow we would have a phase shift of 3 hours. Because of the bottom friction the phase shift becomes about 2 hours. Furthermore, we can see that the current response is skewed from the "non-frictional" sinus function.
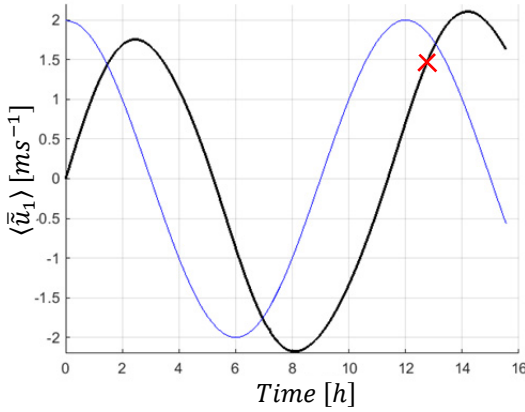

Fig. 6. Black shows the volume averaged velocity from the cosinus type of body forcing used to mimic the tidal forcing at a local position. The red "x" is the time, t_0, when the precursor and Deep Green simulation starts (here the volume avereged velocity is $1.47 \, ms^{-1}$, while the volume avereged velocity for the vertical region the wing spans is $1.58 \, ms^{-1}$). Blue shows the form of the tidal body forcing. Note that the body forcing has another dimension and magnitude, and that it is included here for comparison of the shapes and phase-shift.

The velocity profile, derived from the horizontally averaged velocity as a function of depth at time, t_0, is shown in Fig. 7. We normalize the velocity with the volume averaged velocity $\langle \tilde{u}_1 \rangle_{z,trajectory} = 1.58 \, ms^{-1}$, which is averaged over the depths that enclose the trajectory of the wing. This instance in time is chosen for the analysis since it is used for the initialization of the Deep Green simulation. The mean friction velocity at the bottom for this time is $0.081 \, ms^{-1}$. There is a clear vertical gradient in the horizontally averaged velocity and it resembles to some extent the velocity profiles of a logarithmic layer. This shows that the bottom friction is an important process in the simulations. The velocity gradient over the depths that enclose the wing trajectory is about $0.1 \, ms^{-1}$.
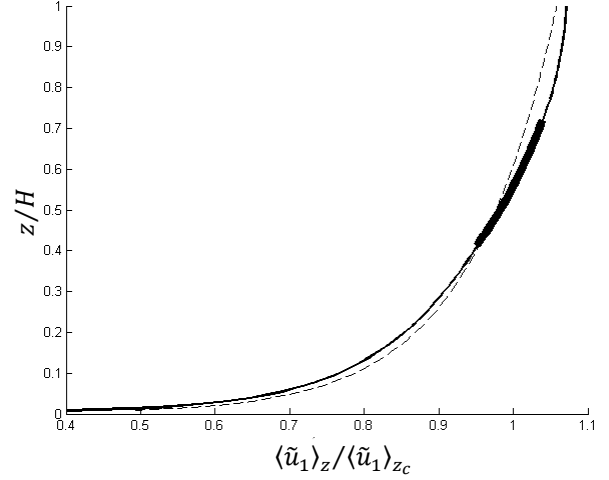

Fig. 7. The horizontally averaged velocity as a function of the depth (thin line). The region of the wing trajectory is indicated by the a thicker line. The dotted line shows the velocity profile of a logarithmic boundary layer flow.

Snapshots of the flow field at a given depth are shown in Fig. 8. This is a small part of the full domain that stretches $4H$ in the y direction and $16H$ in the x direction. We see the elongated scales in the x direction and that the turbulent fluctuations are stronger in $\tilde{u}_1$ than for $\tilde{u}_2$ and $\tilde{u}_3$. In the w-velocity we clearly see that much of the vertical transport seems to be in bursts with high vertical velocities in a small part of the domain.

B. Deep Green

A snap-shot of the flow field from a Deep Green simulation is shown in Fig. 9. This is 300 s after the start of the Deep Green simulation, t_0, which means that approximately 15 full trajectories have passed since the start and that quasi-stationary conditions prevails. The vortices are visualized by isosurfaces of the second invariant of the velocity gradient tensor. This quantity is positive in regions of rotating flow, such as vortices, and is sometimes referred to as the "Q-criterion". The Q criterion is good for visualizing the vortices but the number given for the isosurfaces affects how long downstream the vortices seem to persist before breakdown and is therefore misleading. The strength of the vortices can, however, be compared to the vortices produced by the rough bottom and it is seen that the tip vortices are both stronger and longer than the bottom induced ones and persist fairly long. Another way of discussing the downstream effect is to study the wake in the velocity fields. It is customary to relate the downstream conditions to the distance normalized with a turbine diameter. It is, however, for the Deep Green most likely the wing and its trajectory that dominate the downstream conditions rather than its turbine and therefore some other length scales to be considered are 1) spanwidth S of the wing, 2) full width D_y of the trajectory, and 3) full height D_z of the trajectory. Here the coordinates of the position $1/4$ of the center line chord is used to determine D_y and D_z although the tips of the wing sometimes are further away during the trajectory. In Fig. 9 we present slices of velocity at 1, 2, 3, and 4 times D_y downstream of the point (x_c, y_c, z_c) where the path trajectory crosses its
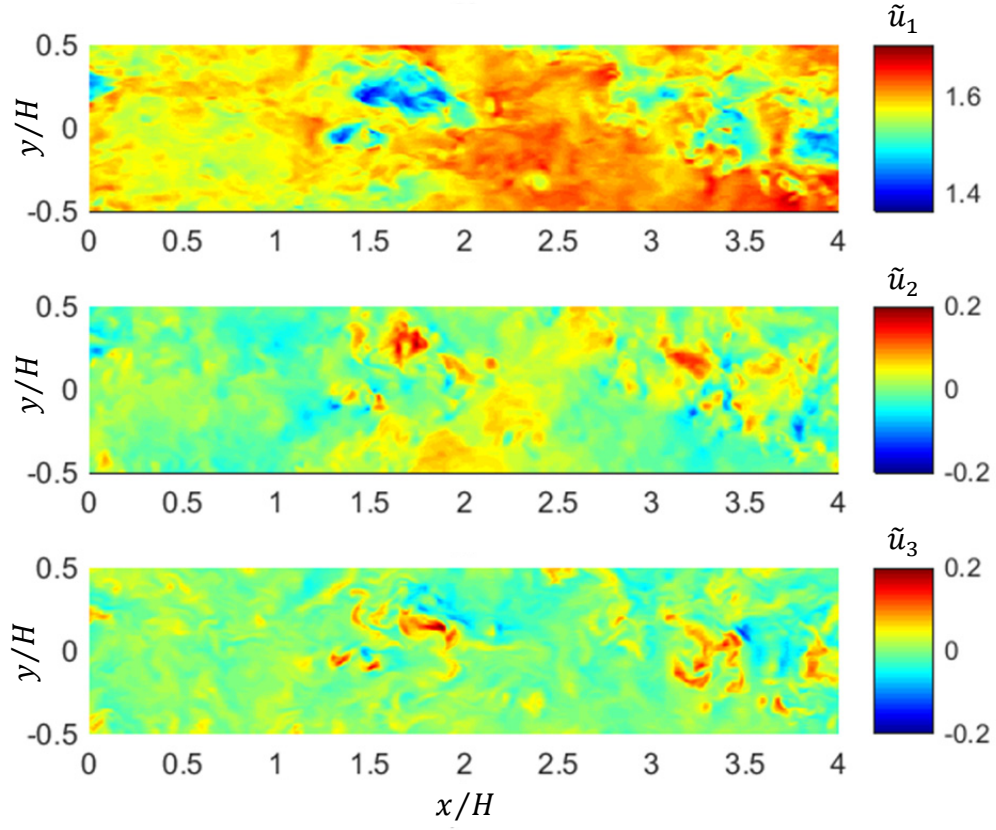
Fig. 8. Instantaneous flow fields at the xy-plane at the center of the trajectory of Deep Green i.e., $z_c = 47.3\ m$ (from bottom), at the time t_0. Note the different color scales in the figures.
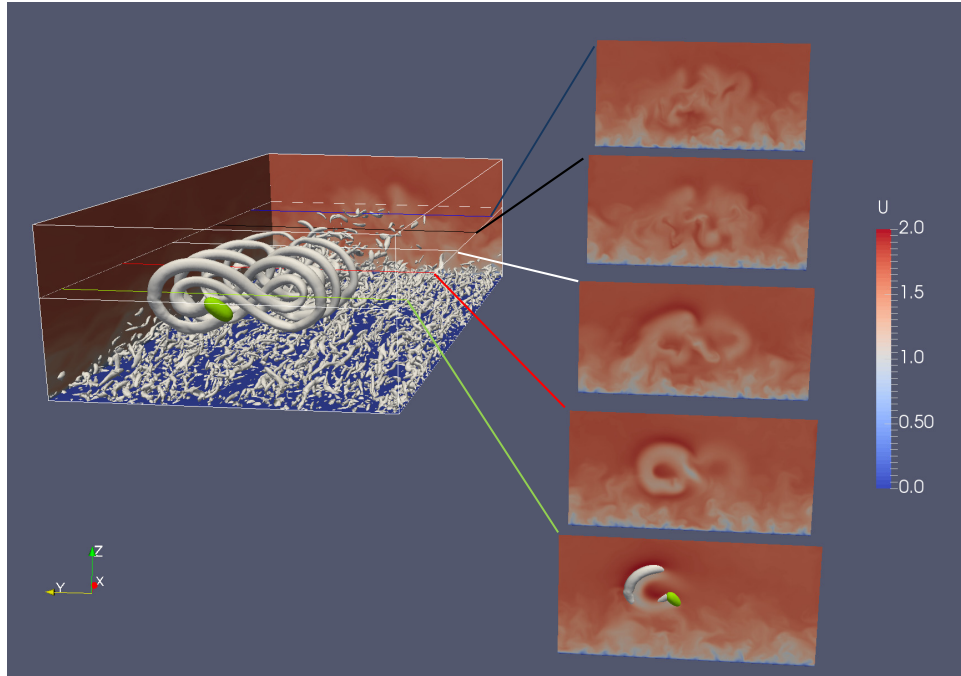

Fig. 9. Instantaneous velocity fields 300 s (15 trajectories) after t_0. Velocities given at domain boundaries at $y = H, x = 4H$, and at yz-planes at $x = x_c, x_c + D_y, x_c + 2D_y, x_c + 3D$, and $x_c + 4D_y$. The grey isosurfaces mark a positive value of the second invariant of the velocity-gradient tensor which indicate vorticies. The position of the Deep Green is vizualized by the green isosurface of the force field.

way. It can be seen that the velocity field is affected at all these distances. Since $4D_y \approx 12D_z \approx 21S$ it is most likely the D_y rather than D_z or S that determines how long downstream the flow is affected. Future simulations with longer computational domain will show how long the actual flow field impact is.

The normalized velocity fields with Deep Green are shown in Fig. 10 for the same instance as in Fig. 9. The horizontal plane is here chosen as $z = z_c$ (which is approximately 2 m above the mean of the max and min of the vertical position of the wing). Here the deviation between the instantaneous velocities and the spatially averaged velocity has been normalized with the spatially averaged velocity as $\underline{\tilde{u}_1} = (\tilde{u}_1 - \langle \tilde{u}_1 \rangle_{z_c})/\langle \tilde{u}_1 \rangle_{z_c}$. It can be seen that the maximum normalized velocity deviations are approximately 40 %. It can also be seen that the deviations are fairly large even at $4D_y$ downstream of the trajectory crossing point.
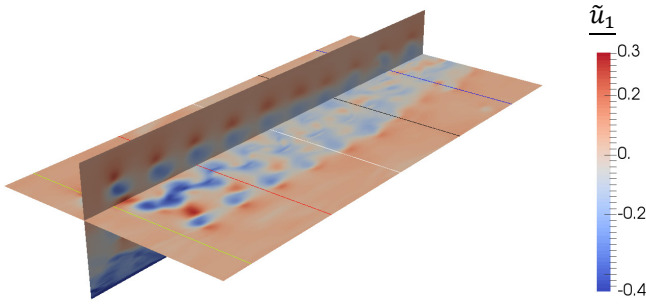

Fig. 10. Instantaneous normalized velocity fields $\underline{\tilde{u}_1}$, 300 s (15 trajectories) after t_0. The velocitiy field is given at the xy-plane at $z = z_c$ and the xz-plane at the y position where the Deep Green trajectory is closest to the surface.

The spatial velocity gradients are an important measure for the control system and the applied fluid forces on the Deep Green. One way of estimating these gradients is to use the magnitude of the vorticity. The normalized magnitude of vorticity $\underline{\tilde{\Omega}} = (\tilde{\Omega} - \langle \tilde{\Omega} \rangle_{z_c})/\langle \tilde{\Omega} \rangle_{z_c}$ is presented in Fig. 11. It can be seen that $\tilde{\Omega}$ is affected all the domain (more than $4D_y$ downstream of x_c).
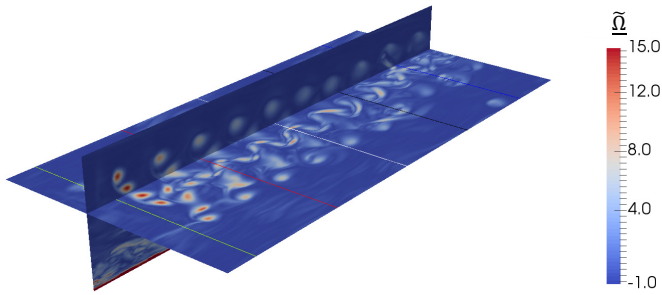

Fig. 11. The magnitude of the vorticity for the instance 300 s after t_0. The vorticity field is given at the xy-plane at $z = z_c$ and the xz-plane at the y position where the Deep Green trajectory is closest to the surface.

The time-averaged streamwise velocity profiles shown in Fig. 12 are useful for the understanding of the wake evolution downstream of the Deep Green. These are taken in the centerline, and downstream of the Deep Green at various locations, similar to Fig. 9. It is seen in Fig. 12a) that the wake is asymmetric in the vertical direction, which is due to the vertical shear in the main flow. It can also be seen in the plot in the horizontal direction, see Fig. 12b) that the wake persists further downstream (at least $4D_y$) for the off-center positions close to the xz-planes at the y position where the Deep Green trajectory is closest to the surface and bottom.
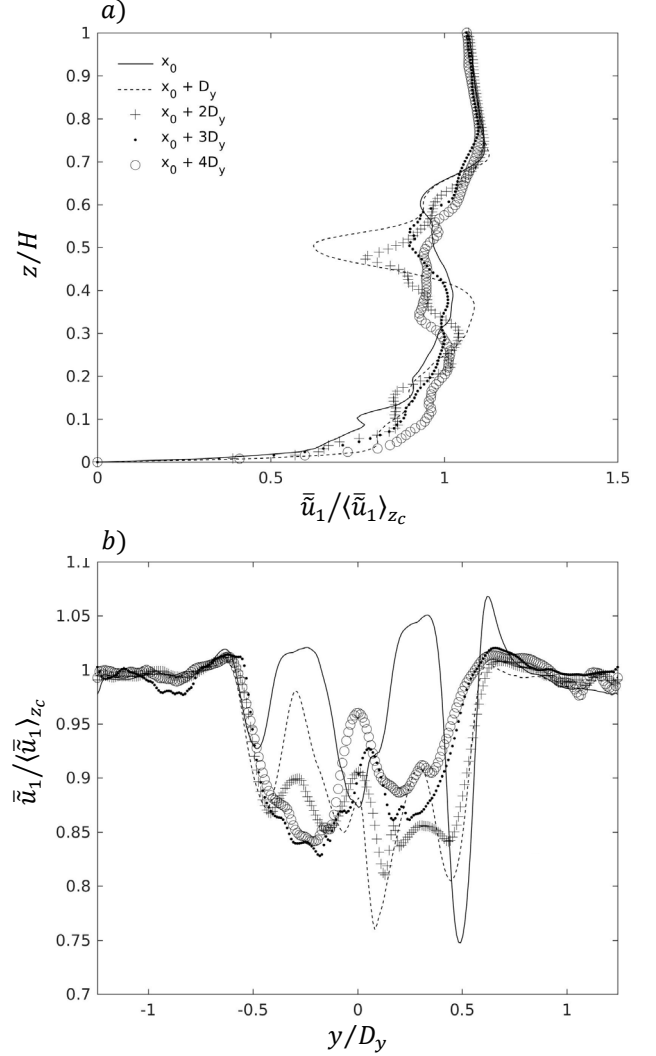

Fig. 12. Velocity deficit comparison at locations downstream of the Deep Green trajectory center (x_c, y_c, z_c). Time averaged over 200-400 s after t_0. a) vertical profiles along the xz-plane at $y = y_c$. b) horizontal profiles along the yz-plane at $x = x_c$

IV. CONCLUSIONS

The overall aim for this work is to find to what extent and how long downstream the Deep Green affect the flow field. This information is e.g., important to be able to optimize the packing of eventual arrays of power plants. The main focus of the present work is to design a numerical framework for studies of the interaction between the Deep Green tidal power plant and the tidal flow, under realistic conditions. A work process is designed, in which a the turbulence of the oscillating tidal flow is predicted using an efficient pseudo-spectral method,

followed by finite volume simulations and the actuator line method to include the effects of the Deep Green power plant on the flow. This ensures that the studies are performed in a realistic turbulent and oscillating tidal flow field.

It is found that the numerical framework and work process are appropriate for the present studies. The numerically predicted undisturbed boundary layer (without the power plant) is comparable to the theory of the law of the wall for a rough bottom boundary condition. Initial studies in the present work show that the turbulence is dependent on the phase of the tidal cycle. The studies with the Deep Green power plant are performed during accelerating flow, close to the maximum flow. The results show that the tip vortices, their residues and the increased velocity fluctuations persist the complete computational domain in the streamwise direction. A preliminary analysis indicates that the trajectory width can be used as the characteristic length scale to estimate the affected distance, and the flow is significantly affected at least four trajectory widths downstream the power plant. This needs to be considered when optimizing and packing eventual arrays of power plants.

Some of the steps in the future are to 1) evaluate the need of a correction for lift and drag coefficients for skew inflow to the power plant wing, 2) evaluate the sensitivity to mesh density, 3) increase the computational domain in the streamwise direction in order to find how far downstream the flow is affected by the power plant.

REFERENCES

[1] D. Magagna, R. Monfardini, and A. Uihlein, "JRC Ocean Energy Status Report 2016 Edition," 2016.

[2] M. Lewis, S. Neill, P. Robins, M. Hashemi, and S. Ward, "Characteristics of the velocity profile at tidal-stream energy sites," *Renewable Energy,* 2017.

[3] A. Mason-Jones, D. O'doherty, C. Morris, T. O'doherty, C. Byrne, P. Prickett, *et al.*, "Non-dimensional scaling of tidal stream turbines," *Energy,* vol. 44, pp. 820-829, 2012.

[4] I. A. Milne, R. N. Sharma, R. G. Flay, and S. Bickerton, "Characteristics of the turbulence in the flow at a tidal stream power site," *Phil. Trans. R. Soc. A,* vol. 371, p. 20120196, 2013.

[5] U. Ahmed, D. Apsley, I. Afgan, T. Stallard, and P. Stansby, "Fluctuating loads on a tidal turbine due to velocity shear and turbulence: comparison of CFD with field data," *Renewable Energy,* vol. 112, pp. 235-246, 2017.

[6] T. Blackmore, L. E. Myers, and A. S. Bahaj, "Effects of turbulence on tidal turbines: implications to performance, blade loads, and condition monitoring," *International Journal of Marine Energy,* vol. 14, pp. 1-26, 2016.

[7] A. Mason-Jones, D. O'doherty, C. Morris, and T. O'doherty, "Influence of a velocity profile & support structure on tidal stream turbine performance," *Renewable Energy,* vol. 52, pp. 23-30, 2013.

[8] K. McCaffrey, B. Fox-Kemper, P. E. Hamlington, and J. Thomson, "Characterization of turbulence anisotropy, coherence, and intermittency at a prospective tidal energy site: Observational data analysis," *Renewable Energy,* vol. 76, pp. 441-453, 2015.

[9] R. J. Barthelmie and L. Jensen, "Evaluation of wind farm efficiency and wind turbine wakes at the Nysted offshore wind farm," *Wind Energy,* vol. 13, pp. 573-586, 2010.

[10] R. J. Barthelmie, S. Pryor, S. T. Frandsen, K. S. Hansen, J. Schepers, K. Rados, *et al.*, "Quantifying the impact of wind turbine wakes on power output at offshore wind farms," *Journal of Atmospheric and Oceanic Technology,* vol. 27, pp. 1302-1317, 2010.

[11] S. B. Roy, "Simulating impacts of wind farms on local hydrometeorology," *Journal of Wind Engineering and Industrial Aerodynamics,* vol. 99, pp. 491-498, 2011.

[12] W. Zhang, C. D. Markfort, and F. Porté-Agel, "Experimental study of the impact of large-scale wind farms on land–atmosphere exchanges," *Environmental Research Letters,* vol. 8, p. 015002, 2013.

[13] G. Broström, "On the influence of large wind farms on the upper ocean circulation," *Journal of Marine Systems,* vol. 74, pp. 585-591, 11// 2008.

[14] M. J. Churchfield, Y. Li, and P. J. Moriarty, "A large-eddy simulation study of wake propagation and power production in an array of tidal-current turbines," *Philosophical Transactions of the Royal Society A: Mathematical,*
        Physical and Engineering Sciences, vol. 371, 2013.

[15] S. W. Funke, P. E. Farrell, and M. D. Piggott, "Tidal turbine array optimisation using the adjoint approach," *Renewable Energy,* vol. 63, pp. 658-673, 2014/03/01/ 2014.

[16] S. R. Turnock, A. B. Phillips, J. Banks, and R. Nicholls-Lee, "Modelling tidal current turbine wakes using a coupled RANS-BEMT approach as a tool for analysing power capture of arrays of turbines," *Ocean Engineering,* vol. 38, pp. 1300-1307, 2011/08/01/ 2011.

[17] R. Malki, I. Masters, A. J. Williams, and T. Nick Croft, "Planning tidal stream turbine array layouts using a coupled blade element momentum – computational fluid dynamics model," *Renewable Energy,* vol. 63, pp. 46-54, 2014/03/01/ 2014.

[18] J. C. McWilliams, E. Huckle, J.-H. Liang, and P. P. Sullivan, "The Wavy Ekman Layer: Langmuir Circulations, Breaking Waves, and Reynolds Stress,"

Journal of Physical Oceanography, vol. 42, pp. 1793-1816, 2012.

[19]   P. P. Sullivan, J. C. McWilliams, and C.-H. Moeng, "A subgrid-scale model for large-eddy simulation of planetary boundary-layer flows," *Boundary-Layer Meteorology,* vol. 71, pp. 247-276, 1994.

[20]   C.-H. Moeng, "A Large-Eddy-Simulation Model for the Study of Planetary Boundary-Layer Turbulence," *Journal of the Atmospheric Sciences,* vol. 41, pp. 2052-2062, 1984.

[21]   S. T. Fredriksson, L. Arneborg, H. Nilsson, and R. A. Handler, "Surface shear stress dependence of gas transfer velocity parameterizations using DNS," *Journal of Geophysical Research: Oceans,* pp. n/a-n/a, 2016.

[22]   P. K. Jha, M. J. Churchfield, P. J. Moriarty, and S. Schmitz, "Guidelines for volume force distributions within actuator line modeling of wind turbines on large-eddy simulation-type grids," *Journal of Solar Energy Engineering,* vol. 136, p. 031003, 2014.

[23]   P. Bachant, A. Goude, and M. Wosnik, *Actuator line modeling of vertical-axis turbines*, 2016.

[24]   C. H. Moeng and P. P. Sullivan, "NUMERICAL MODELS | Large-Eddy Simulation A2 - North, Gerald R," in *Encyclopedia of Atmospheric Sciences (Second Edition)*, J. Pyle and F. Zhang, Eds., ed Oxford: Academic Press, 2015, pp. 232-240.

[25]   E. De Villiers, "The potential of large eddy simulation for the modelling of wall bounded flows," Department of Mechanical Engineering, Imperial College London, 2007.

[26]   J. N. Sorensen and W. Z. Shen, "Numerical modeling of wind turbine wakes," *Journal of Fluids Engineering-Transactions of the Asme,* vol. 124, pp. 393-399, Jun 2002.

[27]   I. H. Abbott and A. E. Von Doenhoff, *Theory of wing sections, including a summary of airfoil data*: Courier Corporation, 1959.